Engineering Journal issn: 0125-8281

Article

The Role of Energy Density in Phase-Microstructure Evolution and Mechanical Properties of Ti-Zr-Cu Alloys Fabricated by Laser Powder-Bed Fusion

Pattarapong Wannapraphai[1,a], **Thanawat Phetrattanarangsi**[1,b], **Surasak Kuimalee**[2,c], **Boonrat Lohwongwatana**[1,d], **and Chedtha Puncreobutr**[1,e,*]

1 Department of Metallurgical Engineering, Faculty of Engineering, Chulalongkorn University, Bangkok, 10330, Thailand
2 Industrial Chemistry Innovation Programme, Faculty of Science, Maejo University, Chiang Mai 50290, Thailand
Email: [a]pattarapong.wan@gmail.com, [b]thanawat.osk128@gmail.com, [c]surasak_k@mju.ac.th, [d]boonrat.l@chula.ac.th, [e,*]chedtha.p@chula.ac.th (corresponding author)

Abstract. Laser powder-bed fusion (L-PBF) additive manufacturing technique offers significant advantages in fabricating Ti-Zr-Cu alloys by enabling precise control over microstructure through process parameter variation. This study investigates the impact of energy density on phase formation, microstructure evolution, and mechanical properties of Ti-Zr-Cu alloys produced from blended elemental powders. By adjusting laser scan speeds to achieve different energy densities, the study reveals that high energy densities result in homogeneous β-(Ti,Zr) phases, while lower energy densities lead to incomplete melting, phase segregation, and inhomogeneous microstructures. Advanced characterisation techniques, including scanning electron microscopy (SEM), energy-dispersive X-ray spectroscopy (EDS), and X-ray diffraction (XRD), were utilised to analyse phase composition and microstructural transformations. Vickers hardness testing demonstrated a correlation between energy density and mechanical properties, with higher energy densities improving overall material hardness. The findings offer valuable insights into optimising L-PBF process parameters for enhanced performance in additively manufactured Ti-Zr-Cu alloys, providing a pathway for advanced applications in biomedical and structural components.

Keywords: Laser powder-bed fusion, Ti-Zr-Cu alloys, energy density, microstructure evolution, hardness.

ENGINEERING JOURNAL Volume 28 Issue 12
Received 18 October 2024
Accepted 12 December 2024
Published 31 December 2024
Online at https://engj.org/
DOI:10.4186/ej.2024.28.12.101

DOI:10.4186/ej.2024.28.12.101

1. Introduction

Additive manufacturing, particularly the laser powder-bed fusion (L-PBF) technique, represents a transformative approach in metal and alloy fabrication. This method offers significant advantages over traditional manufacturing techniques, primarily due to its ability to achieve high cooling rates during the 'layer-by-layer' deposition process. These rapid cooling rates are pivotal in overcoming the long-standing challenges associated with controlling the microstructure and phase distribution in metal alloys, which often affect the material's mechanical properties and performance [1-4]. Historically, the field has predominantly utilised pre-alloyed powders, where each particle embodies the complete chemical composition of the target alloy, as demonstrated in studies of Fe-based [5], Zr-based [6], and Ti-based alloys [7]. This approach, while effective, often incurs high costs due to the complex preparation methods required for pre-alloying and subsequent atomisation into powder form. In contrast, in-situ alloying via L-PBF utilises a blend of pure elemental powders mixed to specific proportions to achieve the desired alloy composition directly during the build process. This method not only reduces material costs but also enhances the flexibility in tuning alloy compositions. To address these economic and process flexibility concerns, in-situ alloying via L-PBF has emerged as a promising alternative. In this method, elemental powders are blended in specified proportions, allowing the alloying process to occur directly during the build. This not only reduces the overall cost of material preparation but also significantly enhances flexibility in tailoring alloy compositions for various applications. The ability to customise the elemental composition of the alloy during fabrication opens new avenues for material innovation, especially for applications requiring specific mechanical, thermal, or chemical properties.

Ti-Zr-Cu alloys have emerged as promising materials due to their unique combination of mechanical properties, including high strength, corrosion resistance, and biocompatibility, making them attractive for applications such as biomedical implants [8-10]. The alloy system is relatively simple compared to other multi-component alloys, facilitating both experimental and computational studies of chemical segregation, phase formation, and microstructural evolution [5, 11, 12]. This simplicity makes the Ti-Zr-Cu system an excellent candidate for investigating the effects of additive manufacturing process parameters on alloy properties. In additive manufacturing, the energy density applied during processing plays a critical role in determining the microstructure and phase composition of the alloy. The energy density, typically controlled by adjusting parameters such as laser power, scan speed, and hatch spacing, directly influences the melt pool dynamics, solidification rates, and thermal gradients, which in turn affect phase formation and microstructure [13, 14]. Understanding the relationship between energy density and microstructural evolution is essential for optimising the additive manufacturing process to achieve desirable properties in Ti-Zr-Cu alloys.

Previous studies have shown that variations in processing parameters significantly impact the microstructural features and phase stability of Ti-Zr-Cu alloys. Gao et al. [8] demonstrated that increasing the energy density during selective laser melting (SLM) of Ti-Zr-Cu alloys led to the formation of a refined microstructure with improved mechanical properties. Similarly, Yan et al. [10] reported that adjustments in processing conditions, such as laser scan speed and laser power, could control the formation of different phases, thereby tailoring the alloy's properties to specific applications. Li et al. [15] showed that optimising the laser energy input could reduce defects and enhance the overall quality of Ti-Zr-Cu alloys. These refining microstructures through the precise control of energy density is essential for enhancing the mechanical performance of Ti-Zr-Cu alloys. The results of previous study highlight the importance of energy input in determining the microstructural characteristics and phase stability of additively manufactured alloys. As the field of additive manufacturing continues to evolve, the state-of-the-art research explore the effects of varying process parameters across a broader spectrum of alloy systems to further enhance our understanding of the complex relationship between energy density, microstructural evolution, and material properties. This focus aligns closely with observations in welding processes, where variations in parameters significantly influence the microstructure of the melted and heat-affected zones, as well as the resulting mechanical properties, highlighting a shared foundation in energy-driven material transformations [16, 17].

However, previous studies have been limited in the range of energy densities investigated, and the effects on microstructure evolution and resulting mechanical properties have not been fully explored. This study investigates the effects of energy density on phase formation, phase composition, and microstructural evolution of Ti-Zr-Cu alloys produced from blended elemental powders via additive manufacturing. Three distinct sets of process parameters were used to vary energy density, and the resulting microstructures and phase compositions were characterised using scanning electron microscopy (SEM), energy-dispersive X-ray spectroscopy (EDS), and X-ray diffraction (XRD). The study of Ti-Zr-Cu alloys extends beyond phase formation, as the microstructure's impact on mechanical properties, such as hardness, is critical for practical applications. Refining microstructures through optimised energy density has been shown to significantly enhance the mechanical performance of these alloys. The interdependence of microstructure, phase stability, and properties necessitates a detailed investigation into the effects of additive manufacturing parameters.

2. Materials and Methods

2.1. Sample Preparation

Commercially pure elemental powders of Titanium (AP&C, Canada), Zirconium (Nanoshel, USA), and Copper (H.C. Starck, Germany) were used as precursor feedstock. Each powder had a purity of over 99 wt.% and was characterised for particle size and morphology using scanning electron microscopy (SEM; Quanta 250 FEG, Thermo Fisher Scientific MA). The powder was assessed using SEM, as shown in Fig. 1(a–c), to confirm its spherical geometry and uniform particle morphologies, characteristics typical of the plasma atomisation process. Particle size analysis was also performed (Mastersizer 3000, Malvern Panalytical, UK). The measured average particle size (D50) is 29.9 μm for Ti, 31 μm for Zr, and 25.5 μm for Cu, making them suitable for processing via laser powder bed fusion additive manufacturing.

The Ti, Zr, and Cu powders were mixed with a ratio of 58.5%, 31.5%, and 10% (at.%) to achieve the alloy composition of $Ti_{58.5}Zr_{31.5}Cu_{10}$ (at.%). The alloy was chosen as it has good glass forming ability and a microstructure of in-situ β phases reinforced metallic glass is to be expected [9, 18]. The powders were mixed using an electric tumbler mixer (Inversina 2L, Bioengineering AG, Switzerland) inside an inert atmosphere for 180 minutes) at a rotational speed of 12 RPM to achieve the desired alloy composition.

2.2. Additive Manufacturing

Specimens with dimensions of 10×10×10 mm³ were additively fabricated using the laser powder-bed fusion technique (Concept Laser 200R, GE Additive, MA) in a high-purity argon atmosphere, with oxygen levels maintained below 0.1%. A laser power of 95 W, a layer thickness of 30 μm, and a hatch spacing of 30 μm were used for all samples. To vary the energy density, the laser scan speed was adjusted in the range of 450 to 3,600 mm/s, resulting in volumetric energy densities (VED) ranging from 20 to 175 J/mm³, referred to as E20, E35, E55, E80, E110, and E175, respectively. The VED was calculated using the following equation:

$$\text{VED} = \frac{P}{v \cdot h \cdot t} \quad (1)$$

where P is the laser power, v is the laser scan speed, h is the hatch spacing, and t is the layer thickness. To investigate the influence of laser scan speed on printability and melt pool mixing behaviour—which directly affects phase formation, microstructural evolution, and mechanical properties—this study focuses on the significant role of laser scan speed in melt pool dynamics, including the Marangoni effect [19-21]. To achieve this, three distinct energy density ranges were defined: low energy density (L-VED) for E20 and E35, medium energy density (M-VED) for E55 and E80, and high energy density (H-VED) for E110 and E175. This systematic approach offers clearer insights into the relationship between process parameters and material performance [22-24]. A chessboard scanning strategy was implemented to minimise residual stresses in the samples. The specimens were successfully printed, as shown in Fig. 1(d).

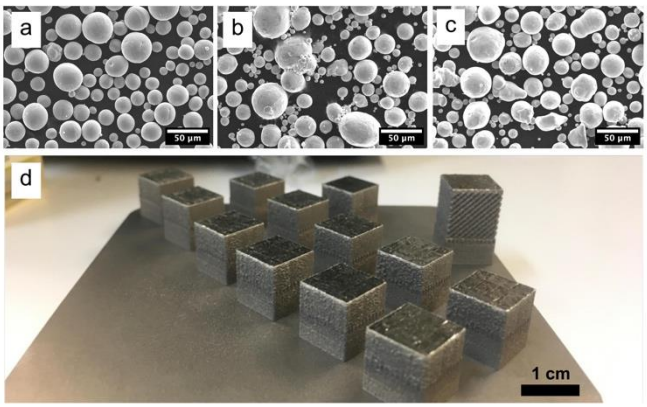

Fig. 1. (a–c) SEM micrographs of Ti, Zr, and Cu elemental powders, respectively, and (d) as-printed specimens.

2.3. Material Characterisation

Phase formation of the fabricated Ti58.5–Zr31.5–Cu10 (at.%) alloy at varying energy densities was analysed using X-ray diffraction (XRD) with a Malvern Analytical diffractometer, utilising Cu Kα radiation over a 2θ range of 20° to 80°, with a step size of 0.02° and a dwell time of 1 second per step. The detected phases were correlated with the energy densities to determine their influence on phase formation.

The microstructure of the as-printed specimens was examined using scanning electron microscopy (SEM) in backscattered electron (BSE) mode at an accelerating voltage of 15 kV. Specimens were prepared using standard metallographic procedures, including sectioning, mounting, grinding, and polishing. BSE images provided detailed insight into phase distribution and morphology, allowing for a comparison of microstructural evolution at different energy densities. Energy-dispersive X-ray spectroscopy (EDS) was employed to determine the chemical composition of the observed phases using point and mapping analysis (Oxford Instruments, UK). Point EDS analysis was conducted on 50 points for each phase across varying regions and energy densities.

Hardness testing of the as-printed samples was conducted using a Vickers hardness tester (MVK-H2 microhardness tester, Mitutoyo, Japan) with a load of 500 gf and a dwell time of 10 seconds. A minimum of 50 indents were made with uniform spacing across each sample, and the average hardness values were calculated. These results were then correlated with the observed microstructures to assess the effect of energy density on the mechanical properties.

DOI:10.4186/ej.2024.28.12.101

3. Results and Discussion

3.1. Phase Formation

The phase formation of all printed specimens was investigated to understand the impact of varying energy densities on phase crystallisation. X-ray diffraction (XRD) analysis was conducted to assess phase formation, and the resulting diffraction patterns for as-printed specimens at different energy densities are shown in Fig. 2.

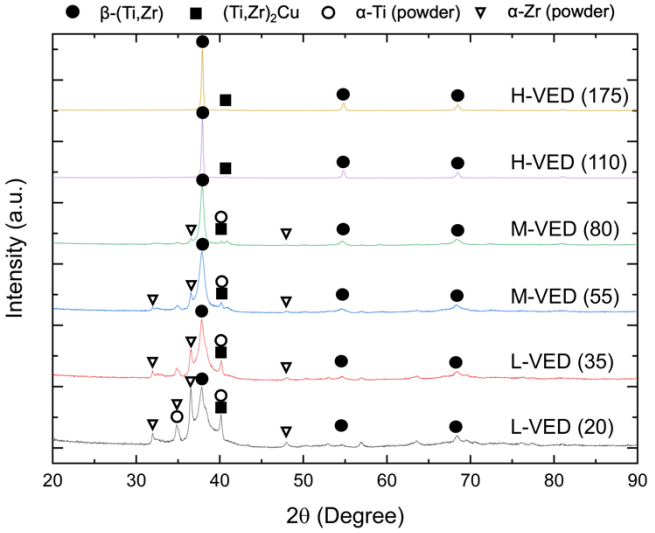

Fig. 2. XRD results of as-printed $Ti_{58.5}Zr_{31.5}Cu_{10}$ (at.%) specimens at varying energy densities.

At high energy densities (H-VED, 110 and 175 J/mm³), the specimens exhibited complete melting and crystallisation, predominantly forming the β-(Ti,Zr) phase (JCPDS no. 00-044-1288) , with a minor presence of the $(Ti,Zr)_2Cu$ phase (JCPDS no. 00-015-0717). It is worth noting that this reference number corresponds to the Ti_2Cu phase, which has a tetragonal lattice structure. In our study, the $(Ti,Zr)_2Cu$ phase is likely to forms with the same tetragonal lattice structure as the Ti_2Cu phase. However, the substitution of Zr atoms for Ti atoms results in a larger lattice structure due to the larger atomic size of Zr. This structural change causes the diffraction peaks shifted compared to the reference pattern. A similar phenomenon of $(Ti,Zr)_2Cu$ phase formation has been reported in studies [8, 9]. This suggests that sufficient energy input facilitates full melting and subsequent crystallisation of the alloy into equilibrium phases. As the energy density decreased to medium levels (M-VED, 55 and 80 J/mm³), the relative amounts of the β-(Ti,Zr) phase and the $(Ti,Zr)_2Cu$ phase slightly diminished, indicating a partial reduction in crystallisation. At lower energy densities (L-VED, 20 and 35 J/mm³), unmelted elemental Ti (JCPDS no. 00-001-1198) and Zr (JCPDS no. 00-001-1147) powders were detected, likely due to insufficient energy input to fully melt these elements, which have high melting points. Additionally, a scattering hump around 30–40° indicates the presence of an amorphous phase. As the energy density decreased, the scattering hump became broader, while the fractions of the β-(Ti,Zr) and $(Ti,Zr)_2Cu$ phases slightly decreased. This suggests that the proportions of crystallised and amorphous phases are influenced by the L-PBF processing parameters, particularly the laser scan speeds used in this study. Gao et al. [8, 9, 18] similarly observed the coexistence of a crystallised β-(Ti,Zr) phase with a metallic-glass matrix microstructure at higher energy densities (VED = 166 J/mm³) in similar Ti-Zr-Cu alloy systems. These findings highlight the crucial role of energy density in determining phase formation and its stability.

3.2. Microstructure Evolution

The microstructural evolution of the as-printed specimens was examined using scanning electron microscopy (SEM) to elucidate the effect of energy density on solidification behaviour. The morphology of the solidified melt pool across different energy densities revealed diverse solidification structures, as shown in Fig. 3. Three primary microstructures were observed: (1) complete melting with chemical homogeneity, (2) complete melting with partial segregation, and (3) partial un-melting with the presence of pure elemental particles.

At H-VED (110 and 175 J/mm³), Fig. 3(a-b) and at higher magnification in Fig. 4(a-b), the melt pool was fully homogenised, yielding well-mixed microstructures dominated by primary β-(Ti,Zr) phase (darker regions) with small fractions of the $(Ti,Zr)_2Cu$ phase localised in the Cu-enriched residual liquid regions (brighter regions). Although the $(Ti,Zr)_2Cu$ phase is too small to be observed clearly from SEM micrograph (reported as nano-size precipitation [9]), its presence is confirmed by the XRD result. Nucleation of the β-(Ti,Zr) phase occurs at the top of the preceding layer, with growth proceeding along the cooling direction from the edge toward the centre of the melt pool, rejecting solute atoms of Cu and Zr into the residual liquid. The Cu-enriched residual liquid regions exhibit three distinct morphologies: spherical, elongated spheres, and network-like structures. These Cu-enriched regions typically form a network dispersed along the boundaries of the β-(Ti,Zr) grains. However, due to the rapid solidification, some portions of the residual liquid resulting from β-(Ti,Zr) growth fail to merge with other segments, leading to the absence of a complete network structure. Consequently, the formation of spherical and elongated spheres of the residual liquid is observed. This resembles structures documented in previous studies [8, 9].

As the energy density decreased to the M-VED range (55 and 80 J/mm³), microstructural segregation became more pronounced. Localised enrichment of Ti and Zr was observed, as confirmed by backscattered electron (BSE) imaging shown in Fig. 3(c-d). Correlating the observed microstructure with the XRD results, it is possible that the enriched residual liquid, after the formation of the crystalline β-(Ti,Zr) phase, subsequently formed Cu-rich phases, including the crystallised $(Ti,Zr)_2Cu$ phase and an amorphous phase. This aligns well with prior works [8, 9] which indicated that the microstructure of Ti-Zr-Cu

primarily consists of the crystalline β-(Ti,Zr) phase and an amorphous phase, with only a minor fraction of the $(Ti,Zr)_2Cu$ crystalline phase. This phenomenon arises from the rapid solidification inherent to the process, which limits the diffusion time of solute elements, leading to non-equilibrium phases. High cooling rates in L-PBF effectively suppress the nucleation and growth of the $(Ti,Zr)_2Cu$ phase, preventing its extensive formation. Consequently, the remaining liquid, which lacks sufficient time for full crystallisation due to rapid solidification, forms an amorphous phase throughout the microstructure. This transition is driven by limited diffusion of solute elements, hindering the complete formation of crystalline phases and creating competition between amorphous phase formation and residual crystallisation, thereby shaping the alloy's microstructure. This phenomenon is attributed to the rapid solidification process [25, 26].

At even lower energy densities (L-VED, 20 and 35 J/mm³), the microstructure became highly inhomogeneous, with partially unmelted Ti and Zr particles, as shown in Fig. 3(e-f). Additionally, the Cu-riched residual liquid network structure became coarser, accumulating in larger quantities. This observation aligns with the XRD results, which indicate that the peaks of the $(Ti,Zr)_2Cu$ phase become more pronounced as the VED decreases from M-VED to L-VED, along with the appearance of Ti element peaks. It is important to note that the melting points of Ti, Zr, and Cu are 1670°C, 1855°C, and 1084°C, respectively. The incomplete fusion of high melting point elements (Ti and Zr) is attributed to insufficient energy input, leading to unmelted particles. This observation is consistent with previous studies, which reported that lower energy input results in inhomogeneous microstructures with residual unmelted particles [27].

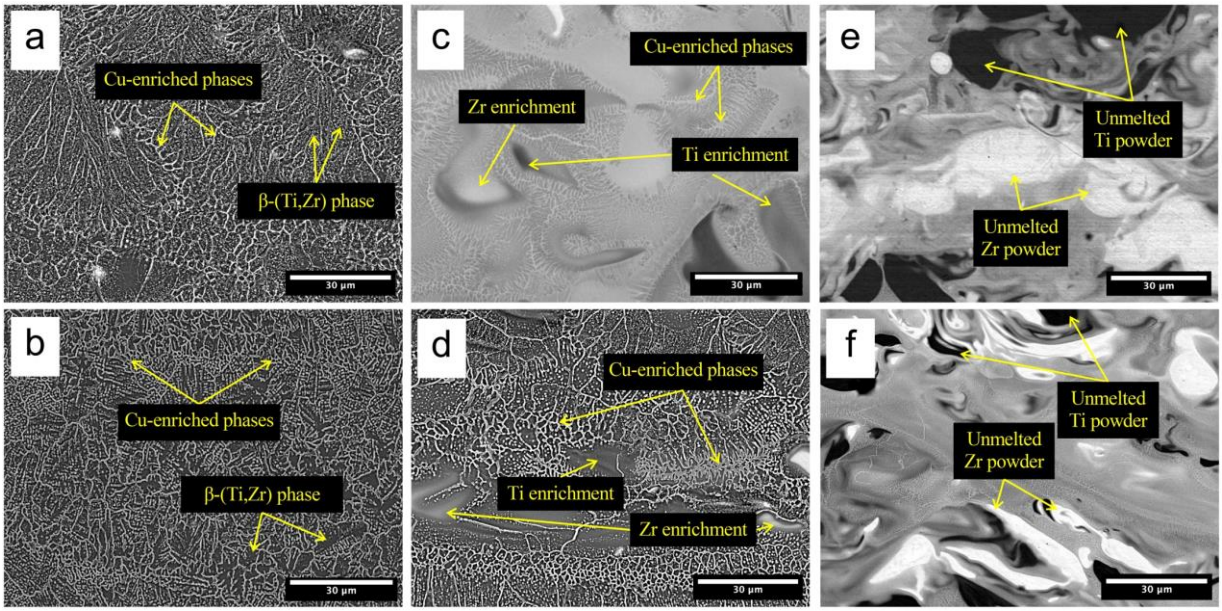

Fig. 3. SEM micrographs of the solidified melt pool at various energy density ranges: (a, b) H-VED range (110 and 175 J/mm³); (c, d) M-VED range (55 and 80 J/mm³); (e, f) L-VED range (20 and 35 J/mm³).

The microstructure evolution study in the high energy density (H-VED) range reveals significant variation in microstructure, influenced by differences in thermal input and cooling rates. As shown in Fig. 4a, at the lower end of the H-VED range (110 J/mm³), columnar β-(Ti,Zr) grains predominantly grew along the cooling direction, extending from the edge toward the centre of the melt pool. These grains were characterised by their small, sharp, and elongated morphology, resulting from rapid solidification and directional heat dissipation. As the energy density increased to 175 J/mm³, the β-(Ti,Zr) grains became larger, with a more equiaxed and less pronounced columnar structure (Fig. 4b). This change is likely due to the higher heat input, which increased the melt-pool size and reduced cooling rates, thereby promoting enhanced mixing of the molten material and longer solidification times. The larger grain size and more equiaxed structure at higher energy densities indicate a shift toward more homogeneous microstructures, with reduced thermal gradients within the melt pool. This agrees with other studies reporting the formation of columnar grains at lower energy densities and the development of more equiaxed grains at higher energy densities, attributed to changes in melt pool dynamics and cooling rates [28-31].

Additionally, the heat-affected zone (HAZ) at the melt pool edge was also influenced by energy density. A wider HAZ was observed at 175 J/mm³ (Fig. 4b as compared to Fig. 4a), consistent with prior studies [32-34]. That showed higher thermal input enlarged the melt pool and expanded the region of thermal influence, increasing interactions between overlapping melt pool layers. This underscores the critical role of laser parameters, particularly energy density, in shaping melt pool geometry and the HAZ in L-PBF processes.

DOI:10.4186/ej.2024.28.12.101

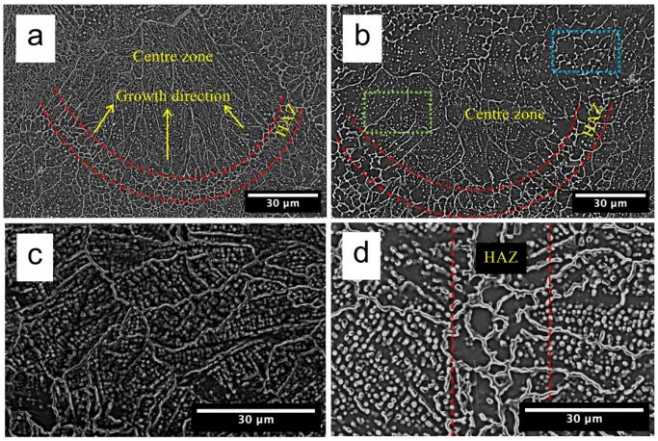

Fig. 4. SEM micrographs of the solidified melt pool. (a) displays columnar β-(Ti,Zr) grains at 110 J/mm³, while (b) shows more equiaxed β-(Ti,Zr) grains at 175 J/mm³, both in the H-VED range. (c-d) illustrate Cu-enriched regions in the centre and edge zones of the melt pool, highlighted in the boxes, respectively.

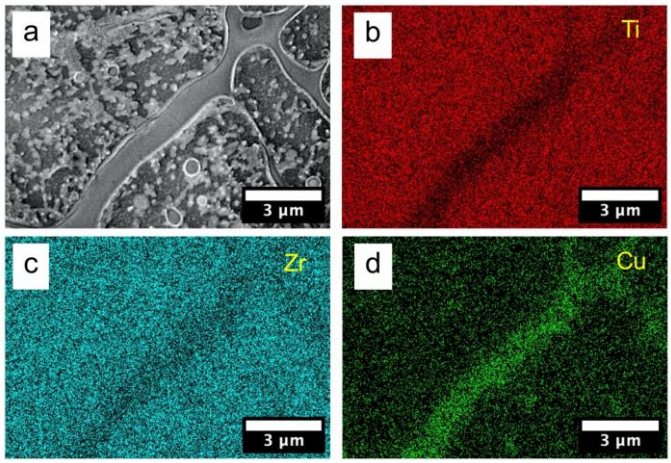

Fig. 5. (a) Micrograph of the solidified melt pool showing the solute-enriched residual liquid regions. (b-d) EDS mapping illustrating the elemental distribution of Ti, Zr, and Cu, respectively.

The centre and edge zones of the melt pool highlight differences in the morphology of Cu-enriched regions, as shown Fig. 4(c-d). In the centre zone, Cu-enriched regions appear as segmented pockets (spherical and elongated spheres) within the β-(Ti,Zr) grains and as a network along β-grain boundaries. Rapid solidification causes some residual liquid to form incomplete network structures. In contrast, the edge zone (i.e. HAZ region) exhibits mainly network-like structures, attributed to remelting between layers. Partial remelting in the edge zone causes the merging of spherical and elongated structures into a network along boundaries of β grains. The EDS mapping of H-VED range (110 J/mm³), as shown in Fig. 5, provides detailed confirmation of the elemental distribution within the melt pool with higher magnification, specifically highlighting the Cu enrichment along the network-like structure at the β-grain boundaries. The mapping also underscores the extent of Cu segregation in these regions, further supporting the observed microstructural differences attributed to remelting and solidification dynamics.

To further analyse the chemical distribution in each phase at varying energy densities, Energy Dispersive Spectroscopy (EDS) analysis was conducted, as detailed in Table 1. Upon solidification, the initial β-(Ti,Zr) phase, with a composition of approximately 60% Ti, 32% Zr, and 8% Cu (at.%), formed first, aligning with previous studies in similar alloy system [8, 9, 18, 35].

As the β-(Ti,Zr) phase grows, Cu and Zr are rejected into the liquid domain, which solidifies as Cu-rich phases at β-grain boundaries or within β-grains. These Cu-enriched regions, showing near-eutectic compositions, predominantly transform into $(Ti,Zr)_2Cu$ or amorphous phases due to the rapid cooling rate. The Cu-rich phases exhibit nearly a 1:1:1 ratio of Ti, Zr, and Cu, with slightly higher Ti and Zr concentrations, as demonstrated in Table 1. This observation aligns with previous studies on the Ti-Zr-Cu alloy system, which reported the composition of the amorphous phase in the β-reinforced metallic-glass matrix microstructure to be close to its deep eutectic composition [8, 9, 18].

It is noteworthy that the chemical variation in the solid phases, confirmed by EDS mapping, is notably high at lower energy densities. This inhomogeneity may possibly result from the Marangoni effect and stirring due to the energy input during the process [19-21]. Additionally, elemental powders used in L-PBF tend to segregate or agglomerate during powder transport and spreading, owing to their varying densities. The combination of non-equilibrium solidification, high cooling rates, and the Marangoni effect could lead to compositional variation, creating separate solid layers with differing compositions during solidification.

The microstructural evolution of Ti-Zr-Cu alloys produced via L-PBF is highly dependent on energy density. High energy densities (H-VED) promote complete melting and sufficient melt-pool mixing, yielding chemically homogeneous microstructures dominated by the β-(Ti,Zr) phase, with localised Cu-rich phases/regions forming network-like structures. Conversely, as energy density decreases (M-VED and L-VED), microstructural segregation becomes more pronounced, resulting in inhomogeneous distributions of Ti and Zr, along with unmelted particles. The formation of Cu-rich phases at lower energy densities further accentuates phase segregation and coarseness within the structure. These variations, confirmed through SEM and EDS analysis, indicate that energy density directly influences both solidification dynamics and phase distribution. Optimising energy input is therefore crucial for achieving microstructural uniformity and controllable phase formation.

Table 1. EDS mapping analysis of phases formed in Ti-Zr-Cu specimens fabricated using varying energy densities in the L-PBF process.

Alloy composition (at.%)	Phase/ Region	Phase/Region Composition (at.%)			VED [J/mm³]	Reference
		Ti	Zr	Cu		
$Ti_{58.5}Zr_{31.5}Cu_{10}$	β-(Ti,Zr)	63.56±12.17	29.46±12.51	7.01±1.78	20 – 35	This work
	Cu-rich phases	44.39±14.71	27.16±14.59	28.44±6.67		
$Ti_{58.5}Zr_{31.5}Cu_{10}$	β-(Ti,Zr)	59.93±12.08	32.02±11.77	8.06±1.90	55 – 80	This work
	Cu-rich phases	44.71±5.83	25.80±4.19	29.50±7.80		
$Ti_{58.5}Zr_{31.5}Cu_{10}$	β-(Ti,Zr)	58.52±1.88	31.98±1.66	9.48±1.18	110 – 175	This work
	Cu-rich phases	39.42±5.59	32.47±4.95	28.10±6.76		
$Ti_{58.5}Zr_{31.5}Cu_{10}$	β-(Ti,Zr)	64.40±2.30	27.40±1.20	8.20±0.60	333	[8]
	Amorphous	34.70±0.30	35.50±1.60	29.80±0.78		
$Ti_{58.5}Zr_{31.5}Cu_{10}$	β-(Ti,Zr)	57.80±0.30	34.20±0.30	8.00±0.01	166	[9]
	Amorphous	31.10±0.10	39.30±0.32	29.60±0.39		

3.3. Mechanical Properties

The candidate specimens formed with energy densities of 35, 80, and 110 J/mm³—representing low (L-VED), medium (M-VED), and high (H-VED) ranges—were tested for mechanical properties using Vickers hardness testing. Since the indentation size (~20 x 20 μm) exceeded the size of individual phases, the measurements reflected the overall hardness of the specimens rather than that of specific phases. A minimum of 50 uniformly distributed indentations were performed on each specimen to ensure statistical reliability. The results, shown in Fig. 6, indicated average hardness values of 380, 404, and 406 HV for low (L-VED), medium (M-VED), and high (H-VED) ranges, respectively. This matches previous findings of 408±10 HV for similar alloys fabricated at a higher energy density [9].

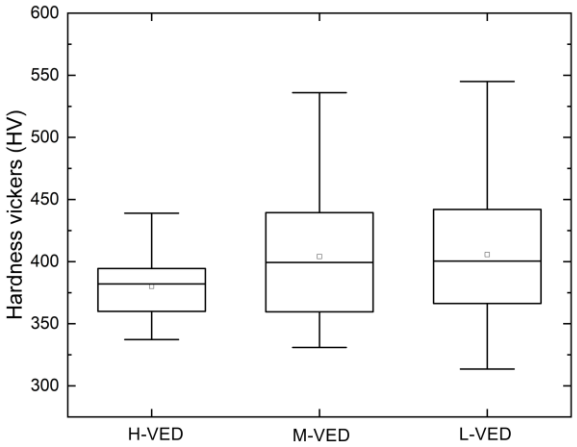

Fig. 6. Vickers hardness results of candidate specimens fabricated using different energy density ranges. The boxes indicated 25 – 75 of percentile of sample space and the upper and lower bar shows the boundaries of hardness value.

Although the average hardness values do not vary significantly across different energy density ranges, the results shown in Fig. 6 indicate that hardness is more consistent in H-VED specimens, with minimal variation. In contrast, L-VED and M-VED specimens exhibit greater hardness variation, likely due to their inhomogeneous microstructures, which consist of regions with differing structures and chemical compositions, as discussed in the previous section. As a reference, the hardness of commercially pure Ti ranges from 200–259 HV, and that of pure Zr ranges from 196–221 HV [36, 37].

This suggests that the presence of unmelted particles reduces hardness, a phenomenon more pronounced under L-VED conditions and gradually diminishing as energy density increases due to melting behaviour is enhanced. This research also found that specimens formed with lower energy densities (L-VED) tend to have slightly higher hardness in certain regions. This may be due to the increased presence of Cu-rich phases, such as $(Ti,Zr)_2Cu$ and amorphous phases, which generally exhibit greater hardness compared to the β-(Ti,Zr) phase. Gao et al. [9] similarly reported that adding Cu content to Ti-Zr-Cu alloys enhances overall hardness. Additionally, the finer microstructure produced by L-PBF contributes to greater hardness and yield strength compared to other methods. This study confirms that hardness varies with energy density, with Cu-rich phases exhibiting higher hardness than β-(Ti,Zr).

Furthermore, this study highlights the impact of volumetric energy density (VED) on the mechanical properties and microstructure of Ti-Zr-Cu alloys manufactured through Laser Powder Bed Fusion (L-PBF). Increasing VED produces more homogeneous and refined microstructures, leading to lower hardness variation and improved mechanical performance. In Ti-Cu systems, higher VED enhances copper dissolution and creates more isotropic microstructures [38], while for Ti6Al4V, it improves grain structure and tensile strength [39]. In Zr-based bulk metallic glasses, optimised VED reduces porosity, increasing hardness and compressive strength [40]. Precise control of VED is crucial for achieving superior alloy properties.

4. Conclusion

This study highlights the critical influence of volumetric energy density (VED) on the phase formation,

microstructural evolution, and mechanical properties of Ti-Zr-Cu alloys manufactured via laser powder bed fusion (L-PBF). High energy densities (H-VED) enable complete melting, leading to a uniform β-(Ti,Zr) phase, minimised phase segregation, and enhanced mechanical properties like consistent hardness. This outcome is attributed to the full melting and mixing of elements, resulting in a homogeneous microstructure dominated by crystallisation of equilibrium phases, supported by optimised heat input and solidification dynamics.

Conversely, at medium (M-VED) and lower (L-VED) energy densities, incomplete melting and phase segregation result in a heterogeneous microstructure with residual unmelted elemental powders. These regions of inhomogeneity lead to varied hardness and reduced mechanical performance. The presence of Cu-rich phases in lower VED specimens further affects mechanical properties, with the hardness increasing locally due to the contribution of the harder $(Ti,Zr)_2Cu$ and amorphous phases.

The microstructure evolution analysis also indicates that the cooling rate and thermal gradients significantly impact grain morphology. At higher VED, grains tend to become larger and more equiaxed, while at lower VED, columnar grain structures predominate, extending along the melt pool cooling direction. This difference in grain morphology, influenced by energy density, affects not only the mechanical properties but also the distribution of solute atoms like copper, which segregate into residual liquid regions during the rapid solidification process.

In conclusion, the findings of this study contribute significantly to the understanding of how additive manufacturing parameters, particularly energy density, affect the final properties of Ti-based alloys. These insights provide a solid foundation for further advancements in the field of additive manufacturing, enabling the production of custom-engineered, high-performance materials for a wide range of applications.

Acknowledgement

The authors acknowledge the financial support through Transforming Systems through Partnership - Thailand project by Royal Academy of Engineering under Newton Fund programme (TSP2021\100366). BL and CP acknowledge Chulalongkorn Academic Advancement into its 2nd Century Project, (Phase 2), Thailand.

References

[1] Z. Yang, M. Markl, and C. Körner, "Predictive simulation of bulk metallic glass crystallization during laser powder bed fusion," *Addit. Manuf.*, vol. 59, p. 103121, 2022, doi: 10.1016/j.addma.2022.103121.

[2] A. A. A. Aliyu, C. Panwisawas, J. Shinjo, C. Puncreobutr, R. C. Reed, K. Poungsiri, and B. Lohwongwatana, "Laser-based additive manufacturing of bulk metallic glasses: Recent advances and future perspectives for biomedical applications," *J. Mater. Res. Technol.*, vol. 23, 2023, doi: 10.1016/j.jmrt.2023.01.184.

[3] C. Zhang, D. Ouyang, S. Pauly, and L. Liu, "3D printing of bulk metallic glasses," *Mater. Sci. Eng. R Rep.*, vol. 145, p. 100625, 2021, doi: 10.1016/j.mser.2021.100625.

[4] H. Lashgari, M. Ferry, and S. Li, "Additive manufacturing of bulk metallic glasses: Fundamental principle, current/future developments and applications," *J. Mater. Sci. Technol.*, vol. 119, no. 131–149, 2022, doi: 10.1016/j.jmst.2021.09.068.

[5] D. Ouyang, W. Xing, N. Li, Y. Li, and L. Liu, "Structural evolutions in 3D-printed Fe-based metallic glass fabricated by selective laser melting," *Additive Manufacturing*, vol. 23, pp. 246-252, 2018, doi: 10.1016/j.addma.2018.08.020.

[6] X. Li, M. Roberts, S. O'keeffe, and T. Sercombe, "Selective laser melting of Zr-based bulk metallic glasses: Processing, microstructure and mechanical properties," *Mater. Des.*, vol. 112, pp. 217-226, 2016, doi: 10.1016/j.matdes.2016.09.071.

[7] L. Deng, S. Wang, P. Wang, U. Kühn, and S. Pauly, "Selective laser melting of a Ti-based bulk metallic glass," *Mater. Lett.*, vol. 212, pp. 346-349, 2018, doi: 10.1016/j.matlet.2017.10.130.

[8] X. Gao, X. Lin, J. Yu, Y. Li, Y. Hu, W. Fan, S. Shi, and W. Huang, "Selective Laser Melting (SLM) of in-situ beta phase reinforced Ti/Zr-based bulk metallic glass matrix composite," *Scripta Mater.*, vol. 171, pp. 21-25, 2019, doi: 10.1016/j.scriptamat.2019.06.007.

[9] X. Gao, X. Lin, Q. Yan, Z. Wang, X. Yu, Y. Zhou, Y. Hu, and W. Huang, "Effect of Cu content on microstructure and mechanical properties of in-situ β phases reinforced Ti/Zr-based bulk metallic glass matrix composite by selective laser melting (SLM)," *Journal of Materials Science & Technology*, vol. 67, pp. 174-185, 2021, doi: 10.1016/j.jmst.2020.06.024.

[10] Q. Yan, J. Yu, X. Lin, M. Dang, S. Shi, Y. Zhang, and W. Huang, "High strength in-situ beta reinforced Ti-based bulk metallic glass composite produced by laser Powder Bed Fusion using elemental powder mixture," *Mater. Sci. Eng. A*, vol. 833, p. 142559, 2022, doi: 10.1016/j.msea.2021.142559.

[11] H. Liu, Q. Jiang, J. Huo, Y. Zhang, W. Yang, and X. Li, "Crystallization in additive manufacturing of metallic glasses: A review," *Addit. Manuf.*, vol. 36, p. 101568, 2020, doi: 10.1016/j.addma.2020.101568.

[12] S. Pauly, C. Schricker, S. Scudino, L. Deng, and U. Kühn, "Processing a glass-forming Zr-based alloy by selective laser melting," *Mater. Des.*, vol. 135, pp. 133-141, 2017, doi: 10.1016/j.matdes.2017.08.070.

[13] R. J. Hebert, "Metallurgical aspects of powder bed metal additive manufacturing," *Journal of Materials Science*, vol. 51, pp. 1165-1175, 2016, doi: 10.1007/s10853-015-9479-x.

[14] T.-I. Hsu, Y.-T. Jhong, and M.-H. Tsai, "Effect of gradient energy density on the microstructure and mechanical properties of Ti6Al4V fabricated by

selective electron beam additive manufacture," *Materials*, vol. 13, no. 7, p. 1509, 2020, doi: 10.3390/ma13071509.

[15] J. Li, Z. Liu, H. Zhou, S. Ye, Y. Zhang, T. Liu, D. Jiang, L. Chen, and R. Zhou, "Effect of process parameters on the microstructure and properties of Cu–Cr–Nb–Ti alloy manufactured by selective laser melting," *Materials*, vol. 16, no. 7, p. 2912, 2023, doi: 10.3390/ma16072912.

[16] M. Masomtob, R. Sukondhasingha, J. Becker, and D. U. Sauer, "Parametric study of spot welding between Li-ion battery cells and sheet metal connectors," *Engineering Journal*, vol. 21, no. 7, pp. 457-473, 2017, doi: 10.4186/ej.2017.21.7.457.

[17] S. Sitthipong, P. Towatana, C. Meengam, S. Chainarong, and P. Muangjunburee, "The influence of parameters affecting mechanical properties and microstructures of semi-solid-metal 7075 aluminum alloy by using friction stir spot welding," *Engineering Journal*, vol. 22, no. 3, pp. 51-64, 2018, doi: 10.4186/ej.2018.22.3.51.

[18] X. Gao, X. Lin, Q. Yan, S. Zhang, J. Lu, T. Zhang, Z. Feng, Y. Tang, and W. Huang, "The in-situ β phase reinforced Ti/Zr-based bulk metallic glass matrix composite by selective laser melting," *Mater. Sci. Eng. A*, vol. 824, p. 141720, 2021, doi: 10.1016/j.msea.2021.141720.

[19] S. A. Khairallah, A.T. Anderson, A. Rubenchik, and W. E. King, "Laser powder-bed fusion additive manufacturing: Physics of complex melt flow and formation mechanisms of pores, spatter, and denudation zones," *Acta Mater.*, vol. 108, pp. 36-45, 2016, doi: 10.1016/j.actamat.2016.02.014.

[20] Z. Gan, H. Liu, S. Li, X. He, and G. Yu, "Modeling of thermal behavior and mass transport in multi-layer laser additive manufacturing of Ni-based alloy on cast iron," *International Journal of Heat and Mass Transfer*, vol. 111, pp. 709-722, 2017, doi: 10.1016/j.ijheatmasstransfer.2017.04.055.

[21] Y.-H. Siao and C.-D. Wen, "Examination of molten pool with Marangoni flow and evaporation effect by simulation and experiment in selective laser melting," *International Communications in Heat and Mass Transfer*, vol. 125, p. 105325, 2021, doi: 10.1016/j.icheatmasstransfer.2021.105325.

[22] Z. Chen, Y. Lu, F. Luo, S. Zhang, P. Wei, S. Yao, and Y. Wang, "Effect of laser scanning speed on the microstructure and mechanical properties of laser-powder-bed-fused K418 nickel-based alloy," *Materials*, vol. 15, no. 9, p. 3045, 2022, doi: 10.3390/ma15093045.

[23] R. Esmaeilizadeh, A. Keshavarzkermani, U. Ali, Y. Mahmoodkhani, B. Behravesh, H. Jahed, A. Bonakdar, and E. Toyserkani, "Customizing mechanical properties of additively manufactured Hastelloy X parts by adjusting laser scanning speed," *Journal of Alloys and Compounds*, vol. 812, p. 152097, 2020, doi: 10.1016/j.jallcom.2019.152097.

[24] A. Soltani-Tehrani, R. Shrestha, N. Phan, M. Seifi, and N. Shamsaei, "Establishing specimen property to part performance relationships for laser beam powder bed fusion additive manufacturing," *International Journal of Fatigue*, vol. 151, p. 106384, 2021, doi: 10.1016/j.ijfatigue.2021.106384.

[25] H. Qin, Q. Dong, V. Fallah, and M. R. Daymond, "Rapid solidification and non-equilibrium phase constitution in laser powder bed fusion (LPBF) of AlSi10Mg alloy: Analysis of nano-precipitates, eutectic phases, and hardness evolution," *Metall. Mater. Trans. A: Phys. Metall. Mater. Sci.*, vol. 51, pp. 448-466, 2020, doi: 10.1007/s11661-019-05505-5.

[26] S. M. Elahi, R. Tavakoli, A. K. Boukellal, T. Isensee, I. Romero, and D. Tourret, "Multiscale simulation of powder-bed fusion processing of metallic alloys," *Computational Materials Science*, vol. 209, p. 111383, 2022, doi: 10.48550/arXiv.2203.10370.

[27] B. Vrancken, S. Dadbakhsh, R. Mertens, K. Vanmeensel, J. Vleugels, S. Yang, and J.-P. Kruth, "Selective Laser Melting process optimization of Ti–Mo–TiC metal matrix composites," *CIRP Ann. - Manuf. Technol.*, vol. 68, no. 1, pp. 221-224, 2019, doi: 10.1016/j.cirp.2019.04.120.

[28] K. V. Yang, Y. Shi, F. Palm, X. Wu, and P. Rometsch, "Columnar to equiaxed transition in Al-Mg (-Sc)-Zr alloys produced by selective laser melting," *Scr. Mater.*, vol. 145, pp. 113-117, 2018, doi: 10.1016/j.scriptamat.2017.10.021.

[29] N. Raghavan, B.C. Stump, P. Fernandez-Zelaia, M. M. Kirka, and S. Simunovic, "Influence of geometry on columnar to equiaxed transition during electron beam powder bed fusion of IN718," *Addit. Manuf.*, vol. 47, p. 102209, 2021, doi: 10.1016/j.addma.2021.102209.

[30] P. Karimi, E. Sadeghi, J. Ålgårdh, A. Keshavarzkermani, R. Esmaeilizadeh, E. Toyserkani, and J. Andersson, "Columnar-to-equiaxed grain transition in powder bed fusion via mimicking casting solidification and promoting in situ recrystallization," *Addit. Manuf.*, vol. 46, p. 102086, 2021, doi: 10.1016/j.addma.2021.102086.

[31] D. Zhang, D. Qiu, S. Zhu, M. Dargusch, D. StJohn, and M. Easton, "Grain refinement in laser remelted Mg-3Nd-1Gd-0.5 Zr alloy," *Scr. Mater.*, vol. 183, pp. 12-16, 2020, doi: 10.1016/j.scriptamat.2020.03.006.

[32] A. Keshavarzkermani, E. Marzbanrad, R. Esmaeilizadeh, Y. Mahmoodkhani, U. Ali, P. D. Enrique, N. Y. Zhou, A. Bonakdar, and E. Toyserkani, "An investigation into the effect of process parameters on melt pool geometry, cell spacing, and grain refinement during laser powder bed fusion," *Optics & Laser Technology*, pp. 11683-91, 2019, doi: 10.1016/j.optlastec.2019.03.012.

[33] S. Shrestha and K. Chou, "Residual heat effect on the melt pool geometry during the laser powder bed fusion process," *Journal of Manufacturing and Materials Processing*, vol. 6, no. 6, p. 153, 2022, doi: 10.3390/jmmp6060153.

[34] S. Nayak, S. Mishra, C. Paul, A. Jinoop, and K. Bindra, "Effect of energy density on laser powder bed fusion built single tracks and thin wall structures with 100 μm preplaced powder layer thickness," *Optics & Laser Technology*, p. 125106016, 2020, doi: 10.1016/j.optlastec.2019.106016.

[35] G. N. Hermana, H.-M. Hsiao, P.-C. Kuo, P. K. Liaw, Y.-C. Li, S. Iikubo, and Y.-W. Yen, "Phase equilibria of the Cu-Zr-Ti ternary system at 703 °C and the thermodynamic assessment and metallic glass region prediction of the Cu-Zr-Ti ternary system," *J Non Cryst Solids.*, vol. 551, p. 120387, 2021, doi: 10.1016/j.jnoncrysol.2020.120387.

[36] S. S. Rocha, G. L. Adabo, G. E. P. Henriques, and M. A. A. Nóbilo, "Vickers hardness of cast commercially pure titanium and Ti-6Al-4V alloy submitted to heat treatments," *Brazilian Dental Journal*, vol. 17, pp. 126-129, 2006, doi: 10.1590/S0103-64402006000200008.

[37] H. M. Qadr, "Effect of ion irradiation on the hardness properties of Zirconium alloy," *Annals of the University of Craiova, Physics*, vol. 29, pp. 68-76, 2019. [Online]. Available: https://www.researchgate.net/publication/338980309_Effect_of_ion_irradiation_on_the_hardness_properties_of_Zirconium_alloy

[38] M. Mosallanejad, B. Niroumand, A. Aversa, D. Manfredi, and A. Saboori, "Laser Powder Bed Fusion in-situ alloying of Ti-5% Cu alloy: Process-structure relationships," *Journal of Alloys and Compounds*, vol. 857, p. 157558, 2021, doi: 10.1016/j.jallcom.2020.157558.

[39] J. Han, J. Yang, H. Yu, J. Yin, M. Gao, Z. Wang, and X. Zeng, "Microstructure and mechanical property of selective laser melted Ti6Al4V dependence on laser energy density," *Rapid Prototyping Journal*, vol. 23, no. 2, pp. 217-226, 2017, doi: 10.1108/RPJ-12-2015-0193.

[40] N. Sohrabi, J. Jhabvala, G. Kurtuldu, M. Stoica, A. Parrilli, S. Berns, E. Polatidis, S. Van Petegem, S. Hugon, and A. Neels, "Characterization, mechanical properties and dimensional accuracy of a Zr-based bulk metallic glass manufactured via laser powder-bed fusion," *Mater. Des.*, vol. 199, p. 109400, 2021, doi: 10.1016/j.matdes.2020.109400.

Pattarapong Wannapraphai, photograph and biography not available at the time of publication.

Thanawat Phetrattanarangsi, photograph and biography not available at the time of publication.

Surasak Kuimalee, photograph and biography not available at the time of publication.

Boonrat Lohwongwatana, photograph and biography not available at the time of publication.

Chedtha Puncreobutr, photograph and biography not available at the time of publication.